On the impact of isotope mass on the stored core thermal energy in JET H-modes

On the impact of isotope mass on the stored core thermal energy in JET H-modes

Plasma Physics and Controlled Fusion

OPEN ACCESS

RECEIVED
14 January 2026

REVISED
24 March 2026

ACCEPTED FOR PUBLICATION
11 May 2026

PUBLISHED
28 May 2026

PAPER

On the impact of isotope mass on the stored core thermal energy in JET H-modes

E Fransson[1,2,*], **L-G Eriksson**[1], **D B King**[3], **H Nordman**[1], **P Strand**[1], **E Viezzer**[4], **D Yadykin**[1], **JET Contributors**[5] **and the EUROfusion Tokamak Exploitation Team**[6]

[1] Chalmers University of Technology, Gothenburg, Sweden
[2] CNRS, Aix-Marseille Univ., PIIM UMR7345, Marseille, France
[3] UKAEA, Culham Campus, Abingdon OX14 3DB, United Kingdom
[4] Department of Atomic, Molecular and Nuclear Physics, University of Seville, Seville, Spain
[5] See Maggi *et al* 2024 (https://doi.org/10.1088/1741-4326/ad3e16) JET Contributors.
[6] See Joffrin *et al* 2024 (https://doi.org/10.1088/1741-4326/ad2be4) the EUROfusion Tokamak Exploitation Team.
[*] Author to whom any correspondence should be addressed.

E-mail: emil.fransson@univ-amu.fr

Keywords: turbulent transport, isotope effect, gyrokinetic, integrated modelling

Abstract

Understanding how the stored thermal energy scales with the main ion isotope, or mixtures of isotopes, in a tokamak is a key question for predicting the performance of future deuterium–tritium operations in ITER and fusion power plants. Although this remains an active area of research, a complete understanding has yet to be achieved. In this study, three JET H-mode discharges with matched engineering parameters are analysed to provide further experimental and analytical input into the investigation of mass scaling of the plasma turbulent transport. The discharges comprise one almost pure hydrogen, one mixed hydrogen–deuterium and one almost pure deuterium plasma. The analysis employs both linear gyrokinetic simulations and an integrated modelling framework. Particular attention is given to three mechanisms through which the mass of the main ion species is expected to influence the core thermal stored energy: (i) the boundary conditions set by the H-mode pedestal, especially in relation to stiff behaviour of temperature and density profiles; (ii) $E \times B$ shearing arising from neutral beam injection driven rotation; and (iii) the contribution of electron temperature gradient-modes to plasma transport. The results presented indicate that the pedestal and $E \times B$ shearing was key in explaining the increased thermal stored energy in the core in the analysed discharges.

1. Introduction

Most present-day magnetic fusion experiments operate with either hydrogen or deuterium plasmas. The fuel mixture for a future fusion reactor, a mixture of deuterium–tritium (DT), has only been tested at significant scale on four occasions, [1–4]. Consequently, the database of DT discharges is limited. It is therefore essential to investigate the scaling of the thermal stored energy of fusion plasmas with the isotope in order to improve predictions for ITER and pilot fusion power plant. In this study, we analyse a set of joint European torus (JET) tokamak discharges that were matched in engineering parameters but employed different main isotopes. The discharges operated in the high-confinement (H-mode) regime, characterised by a temperature and density pedestal near the plasma boundary where turbulence is reduced.

The primary mechanism governing energy and particle transport in tokamak plasmas is microturbulence, which is predominantly driven by radial gradients in plasma temperature and density. In most JET experiments, the instabilities responsible for the highest turbulent transport fluxes are associated with drift waves, particularly the ion temperature gradient (ITG) and trapped electron modes (TEM) [5, 6]. Turbulence is influenced by the mass of the main ion isotope, and the global stored energy in H-mode plasmas has been shown to scale with the effective mass $M_{\mathrm{eff}}^{0.2}$ across a multi-machine

database [7]. Here, M_{eff} denotes the effective mass of the plasma species (e.g. 2 for a deuterium plasma and 1.5 for a 50:50 hydrogen–deuterium plasma). This empirical scaling contradicts the simple dependence of the characteristic length scale, which is dictated by the Larmor radius, $\rho_{\mathrm{L}} \sim \sqrt{M_{\mathrm{eff}}}$. The effect of the normalised Larmor radius, $\rho_* = \rho_{\mathrm{L}}/a$ on the global energy confinement time can be expressed formally as $\tau_{\mathrm{E}} \sim (\rho_*)^{\alpha}\tau_{\mathrm{B}}F(\nu_*, \beta, \ldots)$ [8, 9], where τ_{B} is the Bohm confinement time, F is a function of dimensionless parameters such as the normalised collision frequency ν_* and the ratio of plasma pressure to the magnetic pressure β. Simple drift wave theory would suggest $\alpha = -1$, i.e. gyro-Bohm scaling, leading to a mass dependency $M_{\mathrm{eff}}^{-0.5}$ for τ_{E}, which also means that turbulence driven fluxes should scale as $M_{\mathrm{eff}}^{0.5}$. This is not observed experimentally, indicating that additional mass dependency enters through other mechanisms.

A key factor that could alter the scaling was first proposed by Cordey [10], who suggested that the scaling of the turbulent transport levels could differentiate between the pedestal and the plasma core. Experimentally, it has been well established that the edge plasma in tokamak H-modes exhibits a strong isotope dependence, as observed in JET [11–14], AUG [15, 16], JT-60U [17] etc. A regression analysis of a large JET-ITER Like Wall pedestal database of discharges consisting of hydrogen and deuterium discharges found a significant dependence of the effective mass on the stored thermal energy, scaling as $M_{\mathrm{eff}}^{0.5}$ [11], with both the density and temperature at the top of the pedestal increasing with isotope mass. In the present study, the pedestal acts as a boundary condition, and the effects of its isotope dependence on the turbulent transport in the plasma core are explored.

Several mechanisms within the core transport are also expected to depend on isotope mass. These have been investigated extensively through numerical studies, mainly using non-linear gyrokinetic simulations but also quasi-linear models. These mechanisms include (i) collisions [18]; (ii) $E \times B$-shearing [19–21], (iii) β-effects [22] and the contribution of the electron temperature gradient (ETG)-mode [23]. Another important mechanism is the way in which the pedestal, together with the stiffness of the transport, influences the fluxes [24–26]. As noted earlier, the pedestal height increases with the effective mass, which in turn affects the normalised gradients, e.g. $a/L_X = -a\frac{\mathrm{d}X/\mathrm{d}r}{X}$. Where X represent density or temperature and a is the minor radius. These gradients drive the turbulence, and if the plasma profiles resulting from the turbulence exhibit a stiff behaviour, i.e. the system maintains similar normalised gradients, an increase in density and/or temperature will necessarily lead to higher core gradients ($\mathrm{d}X/\mathrm{d}r$), i.e. peaking.

Another mechanism proposed to influence the isotope scaling of turbulent transport is the strength of zonal flows [22, 27, 28]. The observed isotope dependence may also vary with the dominant instability. For TEM-driven turbulence, collisional stabilisation together with enhanced zonal flow activity has been shown to reduce turbulent transport with increasing ion mass [29]. In contrast, for ITG-dominated plasmas, the turbulent transport exhibits little dependence on isotope mass due to bursty, non-local transport events such as avalanches [30].

To better understand the mechanisms governing isotope scaling of transport strength in H-modes, we have analysed three JET discharges with different isotope compositions. In particular, we have assessed the scaling of core transport coefficients using linear gyrokinetic simulations as well as integrated transport modelling. Special attention is given to the influence of the pedestal height on the core thermal stored energy.

2. Experimental data and modelling setup

This section describes the experimental data and the modelling tools used in the analysis.

2.1. Experimental data

Three discharges from a JET campaign were selected for an in-depth study of the role of isotope mixture on turbulence. The plasmas consisted of hydrogen–deuterium mixtures with effective ion masses $M_{\mathrm{eff}} = 1.18$, 1.79 and 2.13. The discharges were matched in key engineering parameters: plasma current $I_{\mathrm{p}} = 2.3$ MA, toroidal magnetic field $B_{\mathrm{T}} = 2.3$ T and total neutral beam injection (NBI) heating power of 22 MW (no other auxiliary heating sources were applied). This represents a natural way of comparing plasmas with different isotope mixtures. However, a drawback is that the pedestals are not matched. An alternative approach for investigating isotope effects is to maintain constant key dimensionless parameters such as the normalised gyro-radius $\rho_* = \rho/a$, the normalised collisionality, ν_*, normalised gradients and other related dimensionless parameters [31]. The analysed discharges are:

Table 1. Composition and NBI power of the analysed discharges. The percentages are of the electron density and the NBI beams were using deuterium.

Discharge	H (%)	D (%)	Be (%)	Ni (%)	NBI (MW)
97070	89	4	1.6	0.02	22.9
97518	32	60	1.6	0.03	22.5
97064	0	93	1.6	0.02	22.6

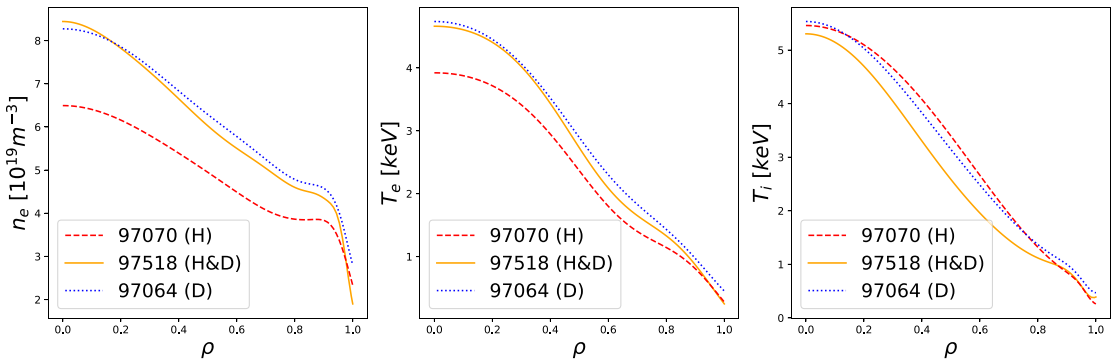

Figure 1. Experimental profiles for the three JET discharges #97070 (H), #97518 (H&D) and #97064 (D). Electrons densities in the left figure, electron temperatures in the middle figure and ion temperatures in the right figure.

- #97070(H), an almost pure hydrogen discharge
- #97518(H&D), a mixed hydrogen and deuterium discharge
- #97064(D), an almost pure deuterium discharge

All three discharges were in H-mode and the plasma heating due to the NBI-deuterium beams strongly dominated over the Ohmic heating. These discharges extend earlier JET studies performed at lower current and magnetic field [32].

The analysis is limited to time intervals when the discharges were in quasi steady state, i.e. when the volume integrated sources and (outward) fluxes were equal at all flux surfaces, and the discharge profiles are relatively fixed. Nevertheless, there were some variations of the profiles with time because of edge-localised modes (ELMs) etc. To minimise their impact, electron and ion profiles were averaged over several ELM cycles. The averaging intervals were: 49–51.8 s for #97070 (H), 50.8–51.6 s for #97518 (H&D), and 49–52 s for #97064 (D).

The resulting experimental profiles of electron density, electron temperature, and ion temperature are displayed in figure 1, with their uncertainties in figure 2. The normalised density and temperature gradients are shown in figure 3 with uncertainties. The data were converted to the integrated data structure (IDS)-format [33] suitable for integrated modelling work flows using the EX2GK tool [34], which applies Gaussian process regression techniques [35]. This statistical approach provides both best-fit profiles and corresponding uncertainty estimates.

Figure 4 presents the averaged toroidal plasma rotation profiles for the time intervals. The uncertainties represent the standard deviation of the data distribution around the mean at each radial position. Notably, the measured toroidal rotation velocities are remarkably similar across all discharges, despite the nearly twofold difference in mass density between the hydrogen and deuterium plasmas and identical NBI settings, same power and species (deuterium).

Details of the plasma compositions are presented in table 1. All discharges contained small amounts of beryllium and nickel impurities, with an effective charge $Z_{\text{eff}} \approx 1.3$. The effective charge was measured by bolometry which provides an average over the plasma core. The hydrogen–deuterium ratio, measured in the divertor, is used as an initial condition in the predictive integrated simulations. For the almost pure hydrogen discharge (#97070), the small deuterium fraction has been neglected.

A global assessment of the variation of the discharge performance with the ion species can be obtained by analysing plasma stored energy. Furthermore, in order to separate the performance of the core plasma from that of the pedestal region, we have calculated the core plasma stored energy separately. The definitions of the core and pedestal stored energy are illustrated in figure 5. As a separation

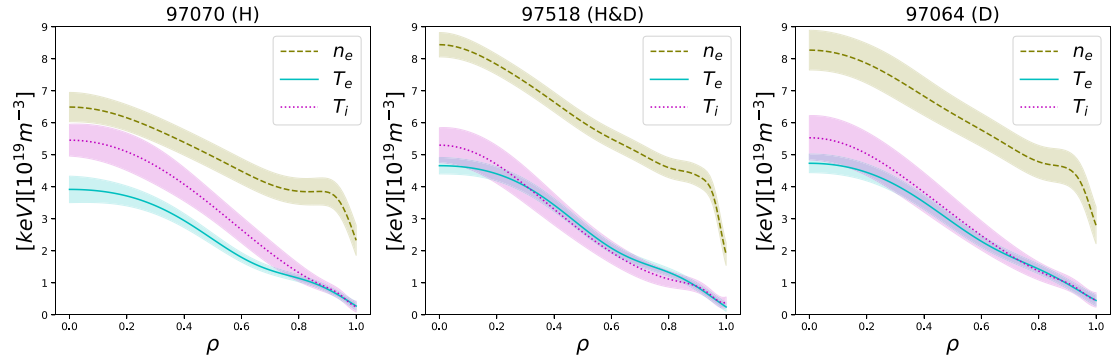

Figure 2. Experimental profiles of the electron density, electron temperature, and ion temperature for the three JET discharges: #97070 (H) (left), #97518 (H&D) (middle) and #97064 (D) (right) with one σ-uncertainty.

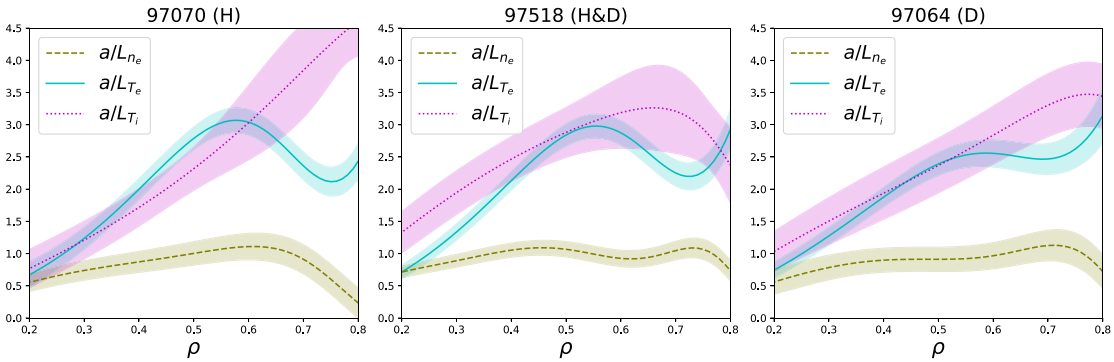

Figure 3. Experimental normalised gradients of the electron density, electron temperature, and ion temperature for the three JET discharges: #97070 (H) left, #97518 (H&D) middle and #97064 (D) right with one σ-uncertainty.

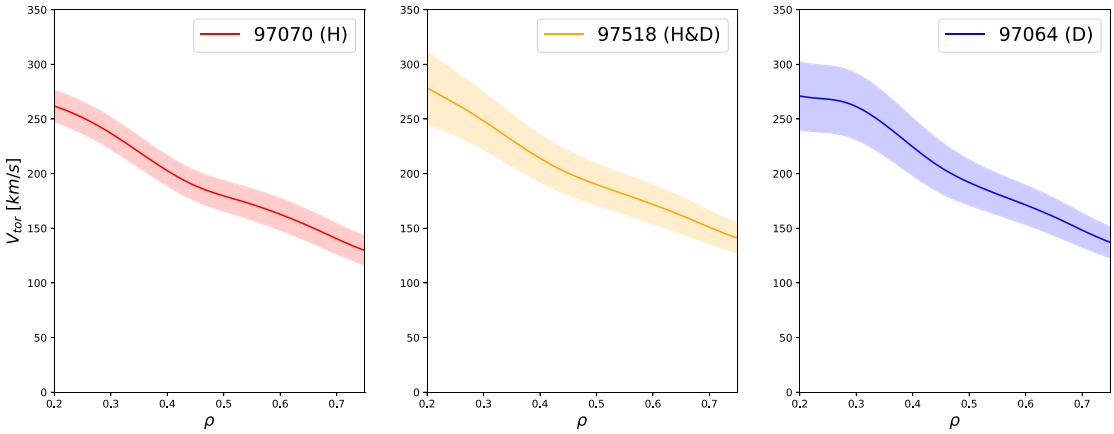

Figure 4. Toroidal rotation velocity for the three discharges: #97070 (H) left, #97518 (H&D) middle and #97064 (D) right, with one σ-uncertainty.

point between core and pedestal, we used $\rho_t = 0.90$ (where ρ_t is the square root of the normalised toroidal magnetic flux). The resulting experimental values for the thermal stored energies are presented in figure 6. The experimental results indicate that both the pedestal and the core thermal stored energy increase as M_{eff} increases. This is consistent with the observations in [17]. The improved core thermal stored energy at increased M_{eff} is the focus of the analysis in this article.

2.2. Modelling setup

The discharges described previously were analysed using both stand-alone turbulent transport codes and an integrated modelling framework.

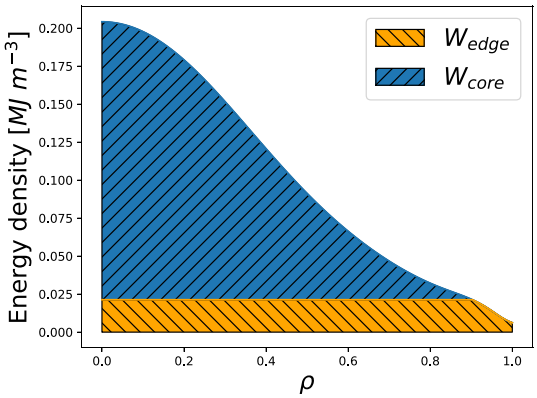

Figure 5. Definition of the thermal stored energy in the edge W_{edge} and in the core W_{core}.

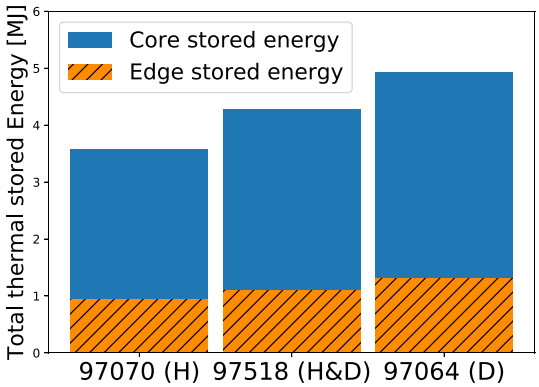

Figure 6. Experimental values for the thermal energy for the three discharges. The thermal stored energy is higher for the discharges with higher M_{eff}, both in the core and the edge. The numerical values are in MJ. #97070(H): Total: 3.57, Edge: 0.93, Core: 2.64. #97518(H&D): Total: 4.28, Edge: 1.10, Core: 3.18. #97064(D): Total: 4.93, Edge: 1.31, Core: 3.62.

2.2.1. GENE setup

Local linear gyrokinetic simulations were performed with GENE [36], which uses an Eulerian δf-method to solve the gyrokinetic Vlasov equation. We have used realistic magnetic equilibrium reconstructed by EFIT [37–39]. Collisions were included via the linearised Landau–Boltzmann operator [40]. All simulations were electromagnetic unless explicitly stated as electrostatic.

2.2.2. ETS setup

Integrated modelling was carried out using the European Transport Solver (ETS) [41, 42]. ETS orchestrates workflows that combine 'building' blocks (individual codes) describing the key processes in the plasma, including equilibrium, plasma transport, and auxiliary heating. The transport equations utilised in ETS describe the evolution of the various bulk plasma profiles, e.g. poloidal flux, densities, and temperatures. Using ETS, we performed predictive simulations of core plasma profiles, starting from experimental profiles and evolving them until steady state was reached.

Turbulent transport within ETS was calculated by the gyro-Landau-fluid code TGLF [43]. TGLF is quasi-linear, solving an eigenvalue problem to obtain growth rates of instabilities, which are combined with the SAT2 saturation model, fitted to non-linear gyrokinetic simulations [44], to evaluate the fluxes. TGLF includes electromagnetic effects, effects of $E \times B$-shearing and kinetic effects, e.g. gyro-averaging, Landau damping. For the simulations in this article, the spectrum, $0.1 < k_\theta \rho_{\mathrm{s,D}} < 24$, was employed where $\rho_{\mathrm{s,D}}$ is the Larmor radius calculated by taking the perpendicular velocity to be equal to the sound speed for deuterium.

Neoclassical transport is included in the ETS simulations via NCLASS [45]. NBI deposition profiles were obtained with the NEMO code [46] and the collisional redistribution of the NBI power density to the bulk ions and electrons was obtained from a simple slowing down model of the NBI induced non-thermal deuterium distribution function. The NBI heating profiles were recalculated at fixed time intervals throughout the simulations to address the evolution of the density and temperature profiles. The

Table 2. Experimental data for the three discharges at the four different radial positions used for the GENE simulations, $\rho_t = 0.5, 0.6, 0.7, 0.8$. The brackets denote flux surface averaged quantities. The $\pm$ denotes one σ uncertainty, also presented in figures 2 and 3. Observe that M_{eff} is calculated without impurities.

ρ_t	(M_{eff})	q	$\hat{s}$	$a/L_{\langle T_e \rangle}$	$a/L_{\langle T_i \rangle}$	$a/L_{\langle n_e \rangle}$	$\nu_{ei}[\frac{c_s}{a}]$	$\langle T_e \rangle$(keV)	$\langle T_i \rangle$(keV)	$\langle n_e \rangle[\frac{10^{19}}{m^3}]$
	97070 (1)	1.27	0.56	2.78 ± 0.18	2.31 ± 0.31	1.00 ± 0.19	0.062	2.36 ± 0.18	3.39 ± 0.44	4.95 ± 0.40
0.50	97518 (1.67)	1.30	0.52	2.85 ± 0.18	2.89 ± 0.39	1.07 ± 0.12	0.080	2.72 ± 0.19	2.58 ± 0.40	6.03 ± 0.30
	97064 (2)	1.18	0.83	2.39 ± 0.18	2.37 ± 0.41	0.91 ± 0.19	0.053	2.89 ± 0.21	3.14 ± 0.54	6.29 ± 0.54
	97070 (1)	1.47	1.04	3.04 ± 0.20	3.03 ± 0.51	1.11 ± 0.22	0.096	1.80 ± 0.14	2.66 ± 0.41	4.49 ± 0.40
0.60	97518 (1.67)	1.49	1.04	2.89 ± 0.19	3.20 ± 0.58	0.92 ± 0.13	0.087	2.09 ± 0.16	1.95 ± 0.35	5.51 ± 0.30
	97064 (2)	1.44	1.40	2.55 ± 0.21	2.83 ± 0.45	0.97 ± 0.20	0.076	2.30 ± 0.18	2.48 ± 0.45	5.78 ± 0.52
	97070 (1)	1.80	1.61	2.36 ± 0.21	3.84 ± 0.64	0.91 ± 0.23	0.14	1.40 ± 0.12	1.94 ± 0.37	4.08 ± 0.40
0.70	97518 (1.67)	1.83	1.60	2.26 ± 0.20	3.22 ± 0.72	1.05 ± 0.15	0.13	1.65 ± 0.14	1.45 ± 0.31	5.05 ± 0.31
	97064 (2)	1.87	1.90	2.46 ± 0.24	3.31 ± 0.48	1.12 ± 0.24	0.11	1.83 ± 0.16	1.87 ± 0.35	5.25 ± 0.51
	97070 (1)	2.31	2.12	2.43 ± 0.27	4.61 ± 0.50	0.23 ± 0.23	0.20	1.14 ± 0.11	1.32 ± 0.26	3.87 ± 0.41
0.80	97518 (1.67)	2.35	2.12	2.93 ± 0.30	2.38 ± 0.61	0.73 ± 0.17	0.18	1.33 ± 0.13	1.12 ± 0.24	4.61 ± 0.31
	97064 (2)	2.44	2.10	3.14 ± 0.44	3.44 ± 0.50	0.72 ± 0.26	0.16	1.43 ± 0.16	1.37 ± 0.27	4.79 ± 0.51

density profiles of impurities have been taken from the experimental measurements and they have been kept fixed throughout the ETS simulations.

As both the turbulent and neoclassical models yield very low transport levels near the magnetic axis-where in reality sawtooth activity dominates-an ad hoc background diffusivity was introduced for $\rho_t < 0.3$. In this central region, an additional diffusivity was set to $\chi = 1.0\ (m^2\,s^{-1})$ in the temperature channels and $D = 0.2\ (m^2\,s^{-1})$ in the particle channels. Consequently, simulation results near the magnetic axis should be interpreted with caution. Furthermore, the simulations have used an internal boundary at $\rho_t = 0.90$, with profiles outside this boundary fixed to experimental values, covering only the region inside the H-mode pedestal.

In the simulations ion and electron temperature profiles were evolved self-consistently. For the almost pure hydrogen discharge, #97070(H), and for the almost pure deuterium discharge, #97064(D), only the electron density was evolved and the main ion density was obtained from the assumption of quasi-neutrality. For the mixed hydrogen–deuterium discharge, #97518(H&D), both the electron and the hydrogen densities were evolved, with the deuterium density determined by quasi-neutrality. The external $E \times B$-shearing profiles used in the simulations were derived from the experimental toroidal rotation velocity profiles and were kept fixed throughout the simulations.

3. Analysis and results

We first examine simulations conducted with the gyrokinetic code GENE, focusing on turbulent transport at specific radial positions in the plasma core, followed by integrated modelling results for the full core region obtained with ETS.

Key physics parameters, including normalised gradients, for the three discharges at four radial positions, $\rho_t = 0.5, 0.6, 0.7, 0.8$, are summarised in table 2. The brackets in the table denote flux surface averaging, defined as:

$$\langle f \rangle (\rho_t) := \frac{\int d^3x f \delta (x - \rho_t)}{\int d^3x \delta (x - \rho_t)}. \quad (1)$$

The parameters across the different discharges are not perfectly matched, which is expected, as the discharges were designed to share the same engineering specifications. Among the parameters, the safety factor exhibits the least relative variation, reflecting the almost identical magnetic field and plasma current. Due to the differences in physical parameters and the known sensitivity of drift-wave turbulence to normalised gradients, disentangling the various factors affecting core transport presents a significant challenge. Nevertheless, by examining one factor at a time, meaningful insights can be obtained.

3.1. Linear instability analysis

For the simulations presented here, GENE was used as an initial value solver, i.e. only the dominant instability at each wave number is determined. Initially, we consider turbulence at ion-scales ($k_y \rho_s < 1.5$); however, when analysing the ETG-modes we also need to consider the electron scales with $k_y \rho_s > 1.5$.

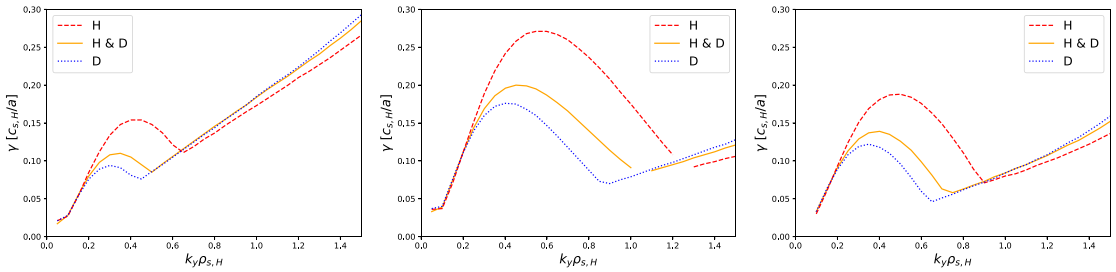

(a) 97070(H) (b) 97518(H&D) (c) 97064(D)

Figure 7. Growth rates for the most unstable mode for the three discharges with changed hydrogen and deuterium mixtures. In (a) we have used the normalised parameters of #97070(H) while changing the isotope mixture. In the same manner we have used the normalised parameters of #97518(H&D) in (b) and #97064(D) in (c) while changing the isotope mixture. Note that the growth rates and wavenumbers are normalised with H, to signify the physical difference of length scales between the simulations.

3.1.1. Effective mass scaling with fixed plasma parameters

To establish the basic mass dependence, linear GENE simulations were performed at $\rho_t = 0.5$ using the three sets of parameters listed in table 2. For each set, three simulations were carried out with M_{eff} corresponding to the three discharges. For example, the normalised parameters of #97070(H) were held fixed while varying M_{eff}. Holding the normalised gradients fixed ensures a consistent comparison. Results are shown in figure 7, with the wavenumber spectrum normalised to ρ_s of hydrogen to emphasise scale differences between isotopes; in all other figures, ρ_s is normalised to the relevant species.

When mass scaling enters only via the Larmor radius-i.e. neglecting collisions and finite β effects-the peak ITG-mode wavenumber and maximum growth rate scale as $k_{\text{peak}}, \gamma_{\text{max}} \sim M_{\text{eff}}^{-1/2}$. Using these two mass dependencies and the mixing length assumption, $\chi \sim \gamma/k_x^2$, where k_x corresponds the wavenumber in the radial direction, we get the relation for the diffusivity, $\chi \sim M_{\text{eff}}^{1/2}$. Despite including collisions and finite β-effects figure 7 shows that the growth rates follow this scaling closely. One should note that the mixing length assumption is a very rough estimate and its compatibility with gyrokinetic simulations can be questioned [47].

In figure 7(a) ETG-modes are strongly destabilised, as indicated by the large growth rates at higher wavenumbers, and may contribute appreciably to the turbulent transport. Their appearance in discharge #97070(H) is linked to a lower $Z_{\text{eff}}T_e/T_i$ which reduces the threshold gradient $(R/L_{T_e})_{\text{critical}}$, for the ETG-mode onset by approximately 30% compared with the other discharges. ETG-mode growth rates are largely insensitive to M_{eff}, though a slight variation at the upper end of $k_y\rho_{s,H}$-spectra arises from the mass dependence of the electron–ion collision frequency. As such they can cause core electron heat transport that does not depend on the ion species, much like TEMs [48]. However, since ETG-modes occur at higher wavenumbers, their overall contribution to core transport is expected to be smaller than their growth rates alone might suggest.

Figure 7 includes finite β effects and collisions which may affect mass scaling through their impact on the non-adiabatic electrons [48, 49]. To isolate their impact on mass scaling, additional simulations were performed for #97070(H) without these effects, see figure 8. In contrast to previous figures we have normalised growth rates and wavenumbers in this figure with species dependent units, i.e. with different M_{eff} of the plasmas. We note the almost perfect alignment of the simulations where finite beta effects and collisions are neglected (figure 8(b)), indicating gyro-Bohm-like scaling. Including collisions and finite-β reduces growth rates but preserves the Larmor-radius scaling, showing that these mechanisms affect amplitude more than fundamental mass scaling.

3.1.2. Simulations using experimental parameters

A second set of linear GENE simulations was performed using the experimentally measured normalised gradients and actual M_{eff} for each discharge, at $\rho_t = 0.5,\ 0.6,\ 0.7,\ 0.8$ (table 2). The results are presented in figure 9, with the left panel of each subplot displaying the growth rate of the fastest growing instability and the right panel their corresponding real frequency. A positive real frequency represents motion in the ion drift direction and a negative one in the electron direction.

ITG-modes dominate at low wavenumbers for all radii, while ETG-modes appear at higher wavenumbers, particularly at $\rho_t = 0.5$ and $\rho_t = 0.6$. Since the normalised gradients differ between discharges, transport scaling does not strictly follow gyro-Bohm; species-unit normalisation would yield overlapping profiles under pure gyro-Bohm scaling. The nearly pure hydrogen and deuterium discharges

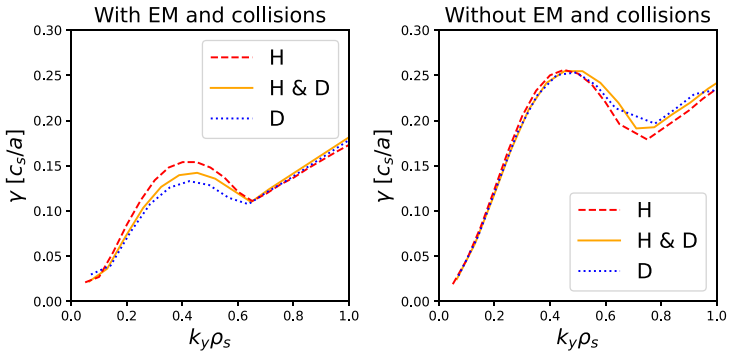

Figure 8. Comparison of the growth rates with and without finite β effects and collisions for the almost pure hydrogen discharge #97070, while changing the M_{eff}. To the left with finite β effects and collisions and to the right without finite β effects and collisions.

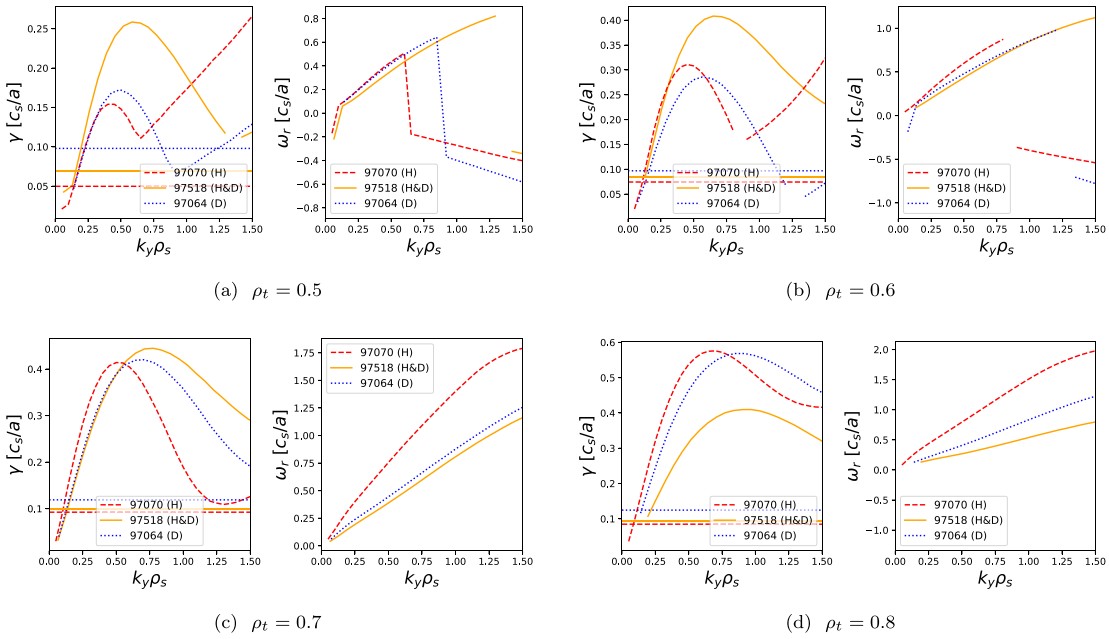

Figure 9. Growth rates and real frequencies for the three discharges, #97070 (H), 97518 (H&D) and #97064 (D) at four different radii. The horizontal lines indicates each discharge external $E \times B$-shearing rate. Note that the growth rates and wavenumbers are normalised with each discharge own M_{eff}.

approximate gyro-Bohm scaling, whereas the mixed hydrogen–deuterium discharge (#97518 H&D) exhibits higher growth rates at the two innermost radii, due to its approximately 20% larger a/L_{T_i}.

These results illustrate that discharges matched in engineering, not physical, parameters are challenging to analyse even with linear theory. Small variations in temperature and density gradients can strongly influence growth rates, highlighting the importance of gradient uncertainties. To further investigate these effects, density and temperature gradient scans were performed, as discussed in the next subsection.

3.1.3. Sensitivity to experimental uncertainties

In order to assess the sensitivity of the growth rates of the modes to variations of the normalised gradients, we have performed linear GENE simulations scanning both a/L_n and a/L_{T_i} simultaneously. This is important because experimental gradients carry non-negligible uncertainties, and small variations could potentially affect the results. Simulations were conducted at mid-radius for a single $k_y\rho_s$ corresponding to the location of the peak growth rate at ion scales found in figure 9(a). $k_y\rho_s$, 0.45 for #97070(H), 0.65 for #97518(H&D) and 0.50 for #97064(D).

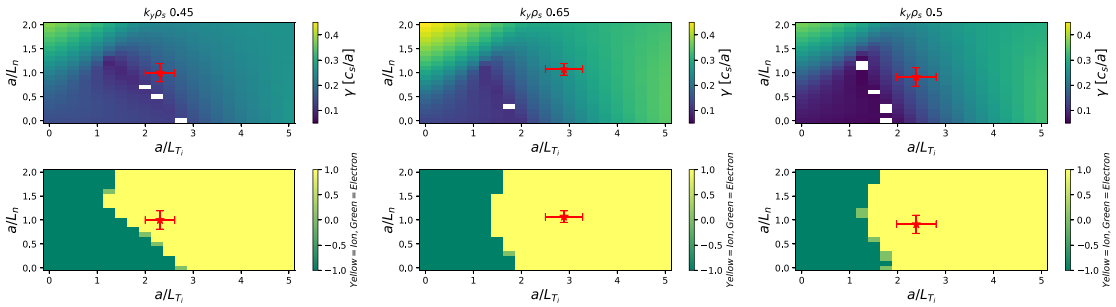

Figure 10. A scan in two dimensions, a/L_{n_e} and a/L_{T_i}, with one fixed wavenumber. The left figure displays result for #97070(H), the middle for #97518(H&D) and the right #97064(D). The top figures display the growth rates and the figures below indicate in which direction the instability is propagating. The wavenumbers for the simulations are taken at the peak for each discharge in figure 9(a), their values are displayed on top of figures. The stars in the figures represent the experimental values and the bars represent the one σ uncertainties in table 2.

The results are displayed in figure 10, with #97070(H) to the left, #97518(H&D) in the centre and #97064(D) to the right. The scans cover from 0 to 2 for a/L_n and from 0 to 5 for a/L_{T_i}. The top subplots display growth rates (normalised to species units), while bottom panels indicate propagation direction: yellow for ion drift, green for electron drift. Red stars mark experimental values, with error bars reflecting uncertainties from table 2. White points in the upper panels and light green points in the lower panels indicate simulations where GENE failed to converge. The bottom panels show that experimental values lie in the ion-drift regime at this radius, corresponding to ITG-modes. The electron-drift regions (green) indicate TEMs, which appear primarily at weak ITGs.

A finer scan around experimental values is presented in figure 11 to confirm ITG dominance within error bars for the mixed discharge #97518(H&D). These simulations again use a single $k_y\rho_s$ and show only growth rates, all modes are propagating in the ion-drift direction, normalised to each species. The mixed discharge exhibits the largest growth rate within the experimental uncertainties.

3.1.4. On the influence of the ETG-mode

The observation that ETG-modes exhibit the highest growth rates in the simulations for discharge #97070(H) at $\rho_t = 0.5$ and $\rho_t = 0.6$ suggests that they may contribute appreciably to the turbulent electron heat flux, even though they occur at smaller spatial scales [50, 51]. The ETG-mode can affect the mass dependency thorough a combination of the ion–electron heat exchange and the stiffness of the ETG mode transport. In heavier isotopes, the transfer of energy from ions to electrons is less efficient, leading to a larger T_i/T_e to be sustained, which suppress the ITG instability [23].

A simple heuristic model for estimating their potential impact is the fraction $\gamma/k_y\rho_s$ which provides an approximate measure of the relative transport contribution. Although recent studies [52, 53] indicate that linear growth rates alone cannot reliably predict the non-linear significance of ETG turbulence, this fraction serves as a practical upper bound for evaluating their influence.

To explore this further, additional linear GENE simulations were performed up to $k_y\rho_s = 50$, to cover the full ETG-mode spectrum. The maximum values of $\gamma_{ITG}/k_y\rho_s$ are compared with $\gamma_{ETG}/k_y\rho_s$ at $\rho_t = 0.5$ in table 3. For the hydrogen discharge #97070(H) the result indicates that the ETG-modes contribution to the turbulent transport could be appreciable while it should be less important for the other two discharges.

To further investigate the importance of ETG modes, we performed stand-alone TGLF simulations at $\rho_t = 0.5$, which include electron-scale turbulence. The simulations indicate a negligible contribution to the fluxes for both the mixed discharge #97518 (H&D) and the deuterium discharge #97064 (D). In contrast, the electron fluxes for the hydrogen discharge, shown in figure 12, exhibit a significant contribution at higher wavenumbers, which are associated with the ETG-mode. These results are consistent with the rough estimates presented in table 3.

3.1.5. Linear assessment of the impact of external $E \times B$-shearing

It is well established that shear in the $E \times B$-velocity breaks up turbulent structures and reduces turbulent transport [54]. The shearing rate is approximately given by,

$$\gamma_{\boldsymbol{E}\times\boldsymbol{B}} \approx \frac{RB_\theta}{B_\phi}\frac{\partial}{\partial r}\left(\frac{E_r}{RB_\theta}\right) \tag{2}$$

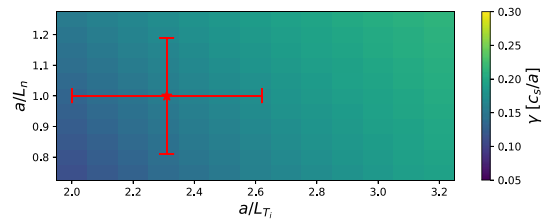

(a) 97070(H), $k_y\rho_s$ 0.45

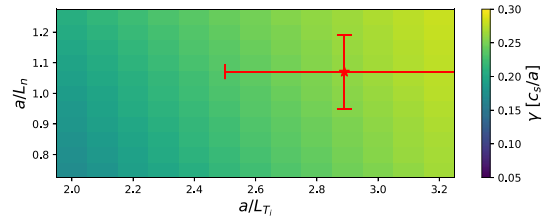

(b) 97518(H&D), $k_y\rho_s$ 0.65

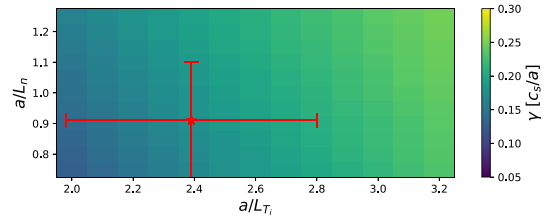

(c) 97064(D), $k_y\rho_s$ 0.50

Figure 11. A scan in two dimensions, a/L_{n_e} and a/L_{T_i}, with one fixed wavenumber. The figures displays the growth rates of the fastest growing instability. This is a finer grid focused around the experimental values compared to figure 10. The error bars around the experimental values are the uncertainties stated in table 2.

Table 3. Test to determine if the ETG-mode has significant contribution to the fluxes by comparing $\gamma/k_y\rho_s$-max at ion- and electron-scales. The result indicate that the ETG-mode is important for #97070(H).

Discharge	$\gamma/k_y\rho_s$-ion	$\gamma/k_y\rho_s$-e	Potential of ETG
97070 (H)	0.44	0.54	High
97518 (H&D)	0.56	0.35	Low
97064 (D)	0.44	0.36	Moderate

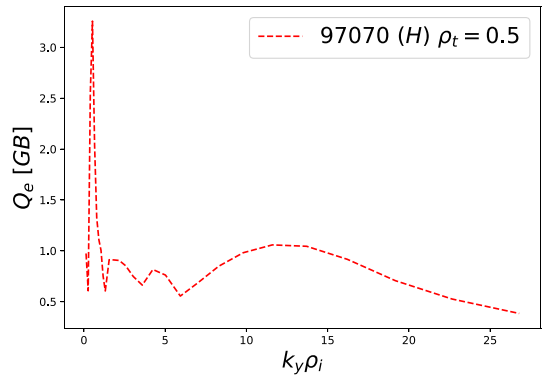

Figure 12. Electron heat flux per wavenumber from a TGLF simulation at $\rho_t = 0.5$ for the hydrogen discharge #97070(H).

E_r is the radial electric field and r is the minor radius in the outer mid-plane of the tokamak. In our study E_r has been obtained from the force-balance equation, with the toroidal velocity component found to be the dominant contributor.

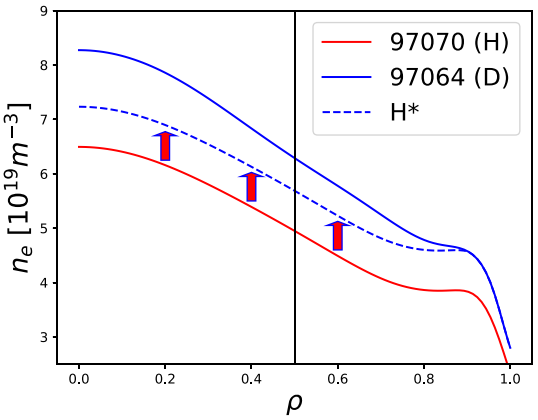

Figure 13. Schematic illustration of the lift of the density profile of the lighter discharge, here #97070(H), such that it has the same value as that of the heaviest discharge #97064(D) at the pedestal top, while keeping the radial derivative inside the pedestal unchanged. This modified profile is denoted as H*. The vertical line indicated the radial position where the linear GENE analysis has been carried out.

As a rule of thumb, the effective growth rate driving the turbulence may be expressed as $\gamma_{\rm eff} = \gamma - \alpha\gamma_{\boldsymbol{E}\times\boldsymbol{B}}$, where γ is the linear growth rate and α is a constant of order unity [55]. Although external $E \times B$-shearing does not alter the linear growth rates themselves, this formulation provides an estimate of its potential influence on the turbulent transport strength. Despite the similar rotation profiles observed across the three analysed discharges (see figure 4) small variations in the shearing rate arise due to differences in the radial gradient of the toroidal rotation.

The linearly calculated growth rates are compared to $\gamma_{\boldsymbol{E}\times\boldsymbol{B}}$ in figure 9 at four radii, $\rho_{\rm t} = 0.5, 0.6, 0.7, 0.8$. The horizontal lines are the $\gamma_{\boldsymbol{E}\times\boldsymbol{B}}$ rates. A rudimentary measure of the factor by which the turbulent transport coefficients should be reduced by the $E \times B$-shearing is $\gamma_{\rm eff}/\gamma = 1 - \alpha\gamma_{\boldsymbol{E}\times\boldsymbol{B}}/\gamma$. For a given $\gamma_{\boldsymbol{E}\times\boldsymbol{B}}$, cases with lower growth rates will therefore experience a stronger relative suppression. As shown in figure 9, the deuterium discharge has the largest ratio $\gamma_{\boldsymbol{E}\times\boldsymbol{B}}/\gamma$ at the innermost radii, implying the most significant reduction in turbulent transport.

In an isotope scan where the plasma parameters-such as the normalised gradients and Larmor radius-are held fixed, the heaviest isotope mixture is always expected to exhibit the lowest growth rate. As demonstrated in figure 7. Therefore, external $E \times B$-shearing under such conditions contributes to a positive scaling with isotope mass of the stored energy in the core plasma.

3.1.6. Influence of the pedestal on the core turbulence

The normalised density and temperature gradients ($a/L_{T_{\rm i,e}} = -a({\rm d}T_{\rm i,e}/{\rm d}r)/T_{\rm i,e}$ and $a/L_{n_{\rm i,e}} = -a({\rm d}n_{\rm i,e}/{\rm d}r)/n_{\rm i,e}$) play a central role in driving drift wave driven turbulence. Consequently, variations in pedestal height are expected to influence the strength of core turbulence transport. It is well established that the pedestal exhibits a clear isotope dependence, with the thermal stored energy increasing with ion mass [11]. Here, we examine how this isotope-dependent pedestal variation impacts core turbulence through linear GENE simulations.

In this analysis, the density and temperature profiles of the two discharges with the lowest $M_{\rm eff}$ (#97070(H) and #97518(H&D)) were artificially raised such that their pedestal heights matched that of the higher-$M_{\rm eff}$ discharge #97064(D), while keeping unchanged radial derivatives (${\rm d}n_{\rm i,e}/{\rm d}r$, ${\rm d}T_{\rm i,e}/{\rm d}r$) inside the pedestal. An example of this procedure is displayed in figure 13. The modified profiles are denoted H* and H&D*, respectively. It should be noted that the present analysis only examines the immediate effect of pedestal lifting on linear growth rates (the actual effect of the stiffness on the profiles cannot be assessed by linear simulations). From figure 13 we can see that H* has lower normalised gradients than its original counterpart, as all profiles are raised with this procedure. The same is true for H&D*. Linear GENE-simulations at $\rho_{\rm t} = 0.5$ were performed for these modified-profiles. The change in the density is 0.72 ($10^{19}{\rm m}^{-3}$) for H* and 0.22 ($10^{19}{\rm m}^{-3}$) for H&D*. For the temperatures, the change is around 0.13 (keV) for both cases.

The results, presented in figure 14, show that both H* and H&D* display lower maximum growth rates than their original counterparts (red/orange solid lines), consistent with the reduced normalised density and temperature gradients. This finding suggests that the higher pedestal associated with larger $M_{\rm eff}$ promotes steeper core profiles by reducing the core turbulence drive. Exactly how this linear effect influences the plasma profiles cannot be determined from the linear analysis alone; integrated modelling

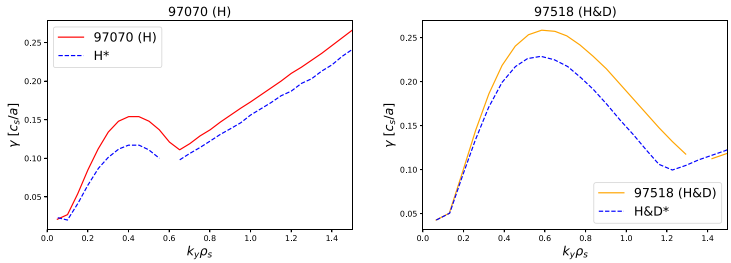

Figure 14. Growth rates for #97070(H) (left, red line) and #97518(H&D) (right, orange line), and for the case where pedestal values have been changed to the ones of #97064(D) discharge, dotted blue lines.

is required. In particular, effects relating to stiff behaviour of the plasma profiles, which are frequently observed in experiments [56], are examined in more detail in section 3.2.

3.1.7. Linear to integrated modelling

In this section we have presented an extensive analysis of the three discharges to assess how the isotope mass affects plasma turbulence.

- **Mass scaling at fixed plasma parameters**: When all plasma parameters are held constant, the growth rates and peak wavenumbers of ITG modes follow gyro-Bohm scaling ($M_{\text{eff}}^{-1/2}$). This implies diffusivity scaling as $\chi \propto M_{\text{eff}}^{1/2}$. Finite-$\beta$ and collisional effects slightly reduce growth rates but do not alter this basic scaling.
- **Simulations using experimental parameters**: Using actual experimental gradients, ITG modes dominate at ion scales ($k_y\rho_s < 1.5$), while ETG modes appear at higher wavenumbers. The mixed H–D case shows somewhat higher growth rates due to steeper ion normalised temperature gradients, highlighting the sensitivity of results to small gradient variations.
- **Sensitivity to uncertainties**: Scans of normalised density and ITGs show that modest experimental uncertainties can shift instability regimes between ITG and TEMs, though ITG remains dominant in the studied cases.
- **ETG-mode influence**: In the hydrogen discharge, ETG modes are particularly strong and contribute to electron heat transport. This effect diminishes with increasing isotope mass.
- **Effect of external $E \times B$ shear**: The $E \times B$ shearing rate, derived from measured toroidal rotation, can suppress turbulence. Since heavier isotopes yield lower growth rates, the relative stabilising effect of $E \times B$ shear is stronger for deuterium, enhancing confinement at higher mass.
- **Pedestal influence**: Artificially raising the pedestal heights, as shown in figure 13, reduces linear growth rates in the core by lowering normalised gradients, indicating that the isotope dependence of the pedestal strongly impacts core turbulence.

The linear analysis indicates two main contributors to the increased thermal stored energy in the core: the external $E \times B$ shear and the pedestal effect. However, these are purely linear results and can only provide an indication of the relative strength of these mechanisms. Non-linear turbulence dynamics and the complex interdependence of the plasma profiles make it difficult to assess their actual impact. Consequently, integrated modelling is required to determine whether these linear effects have a significant influence on the plasma profiles.

3.2. Integrated modelling

In this section we present the self-consistent, integrated simulations of the entire plasma core.

Before presenting the results of the predictive simulations we display the initial profiles of deposited particles and NBI power distributed to ions and electrons after collisional redistribution in figure 15. The NBI heating profiles are broadly similar across the three discharges, although minor differences exist. For instance, the lower pedestal density in #97070 (H) allows deeper beam penetration than in the other two discharges. Furthermore, the critical energy for collisional power exchange decreases with increasing isotope mass, leading to slightly higher electron heating in the deuterium discharge (#97064 D). Overall, the fraction of NBI power transferred to ions was 66 % for #97070 (H), 63 % for #97518 (H&D), and

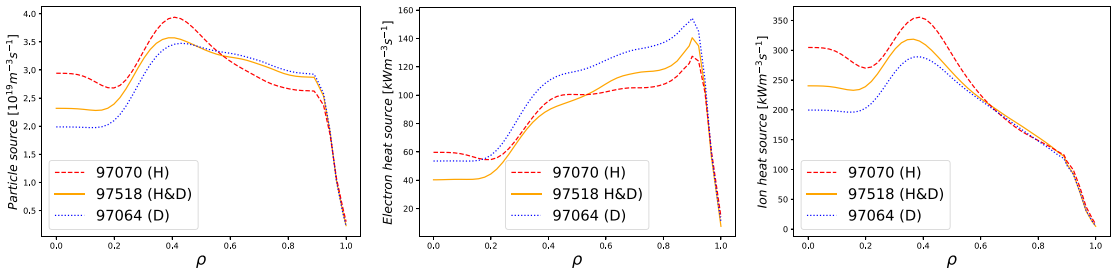

(a) Electron particle source (b) Electron heat source (c) Ion heat source

Figure 15. Distribution of particles and heat from the NBI.

Table 4. Experimental and ETS values for the thermal energy for the three discharges in the core. The uncertainties are an estimate from the uncertainties of the densities and temperatures.

Discharge	Exp. W_{core} (MJ)	ETS W_{core} (MJ)
97070 (H)	2.64 ± 0.27	2.40
97518 (H&D)	3.18 ± 0.27	2.64
97064 (D)	3.62 ± 0.40	2.85

59.5 % for #97064 (D). Although these differences are modest, they introduce some uncertainty in direct comparisons between discharges.

3.2.1. Stored thermal energy

Let us now turn to the outcome of the simulations in terms of plasma performance. The stored plasma energies calculated from the ETS simulations and experimental values are presented in table 4. Encouragingly, the simulations reproduce the experimental trend, with an increasing core thermal stored energy with M_{eff}, although somewhat weaker. The thermal stored energy in the core scales for the experimental profiles as $\sim M_{\text{eff}}^{0.45}$ and for the ETS simulations as $\sim M_{\text{eff}}^{0.24}$.

Figures 16, 17 and 18 compare the experimental and simulated temperature and density profiles. The experimental data are shown as black dotted lines, while the green solid lines represent ETS simulations including external $E \times B$-shear (labelled rot $= 1$), and the red lines correspond to simulations without shear (rot $= 0$). The values in table 4 represent the ETS simulations with $E \times B$-shear. For the two discharges with highest M_{eff}, #97518(H&D) and #97064(D), TGLF slightly underpredicts the densities and cannot replicate the experimental density peaking, even with $E \times B$-shear.

One possible explanation for the somewhat under-predicted core profiles in the analysed discharges is the presence of fast ions and that ETS does not properly account for their effects on the transport. The three discharges contained a non-negligible fast-ion population because the 22 MW of NBI heating. Fast ions may strengthen zonal flows, e.g. through their interaction with fast ion driven toroidal Alfvén eigenmodes, thereby reducing turbulent transport significantly [21, 57]. This is a non-linear effect, which is not included in TGLF version used for the current analysis. Because all three discharges had the same amount of NBI heating power, they should have had a similar fast ion pressure profiles and the effect of the fast ions should then have been similar in all of them. Hence, one would not expect the presence of fast ions to affect scaling with isotope per se. Instead, the core thermal energy for all three discharges should have increased by a similar amount (i.e. if the fast ion effects could have been included in the simulations the core stored energies would have been higher and closer to the experimental values presented in table 4.

In order to assess the contribution of ETG-modes to the transport, we performed in section 3.1.4 stand-alone TGLF simulations at $\rho_t = 0.5$ using the experimental profiles shown in figures 16, 17 and 18. Among the cases considered, only the hydrogen discharge #97070(H) exhibited a significant contribution to the electron heat flux. To evaluate whether ETG-modes influence the quasi steady-state profiles predicted by ETS, we carried out additional stand-alone TGLF simulations using the ETS predicted profiles in figures 16, 17 and 18 (green profiles, labelled rot $= 1$, are with $E \times B$ shear; and red profiles labelled rot $= 0$ are without). In these simulations, neither of the three discharges showed a significant ETG-mode contribution. Thus, this result goes somewhat counter to the stand-alone simulation in section 3.1.4 for the hydrogen discharge #97070 (H). However, there are small differences in the profiles

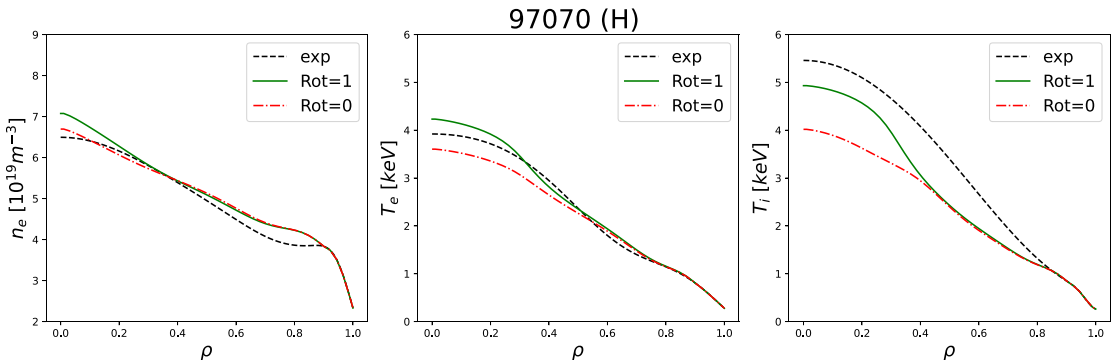

Figure 16. Predictive simulations with ETS for the almost pure hydrogen discharge #97070(H). Exp. is the experimental profile from the quasi steady state and two ETS simulations with and without external $E \times B$-shearing (rotation).

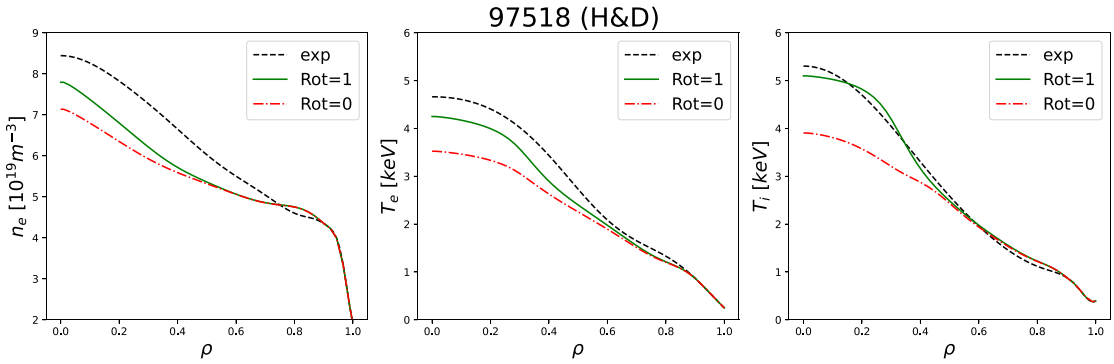

Figure 17. Predictive simulations with ETS for the mixed hydrogen and deuterium discharge 97518. Exp. is the experimental profile from the quasi steady state and two ETS simulations with and without external $E \times B$-shearing (rotation).

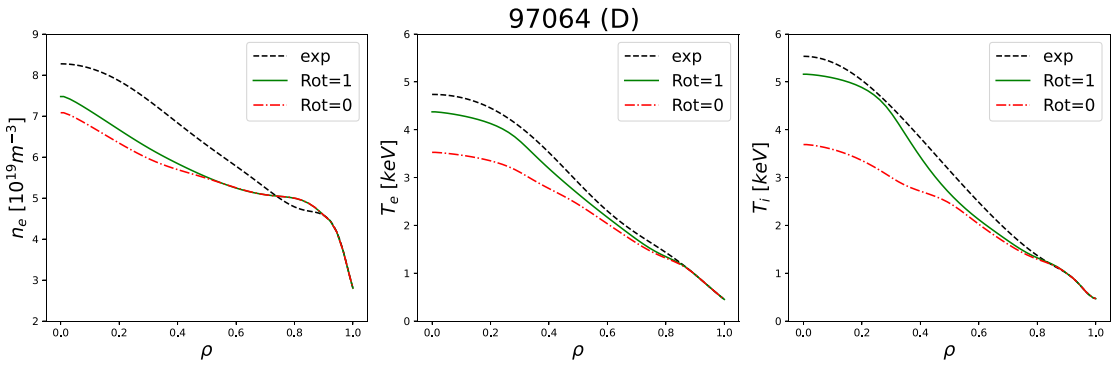

Figure 18. Predictive simulations with ETS for the almost pure deuterium discharge 97064. Exp. is the experimental profile from the quasi steady state and two ETS simulations with and without external $E \times B$-shearing (rotation).

used as input to the calculation in section 3.1.4 and the self-consistently evolved profiles obtained with ETS in figures 16, 17 and 18, which suggests that the profiles were close to the threshold for exciting an ETG mode. Hence, it may be that the ETG mode was not present in the stand-alone TGLF simulations with the ETS predicted simulations because the profiles fell just below the threshold. The presence of a significant ETG-mode in only one of the discharges indicates that it does not play a major role in the positive mass scaling reported in table 4. Furthermore, ETG-modes contribute only in the subdominant electron heat transport channel.

3.2.2. Role of $E \times B$-shearing

The influence of external $E \times B$-shearing can be evaluated by comparing the two ETS cases. Significant differences are observed between the simulations with and without $E \times B$-shearing for all of the three discharges, with the effect being most pronounced for the deuterium case (#97064(D), in figure 18). This

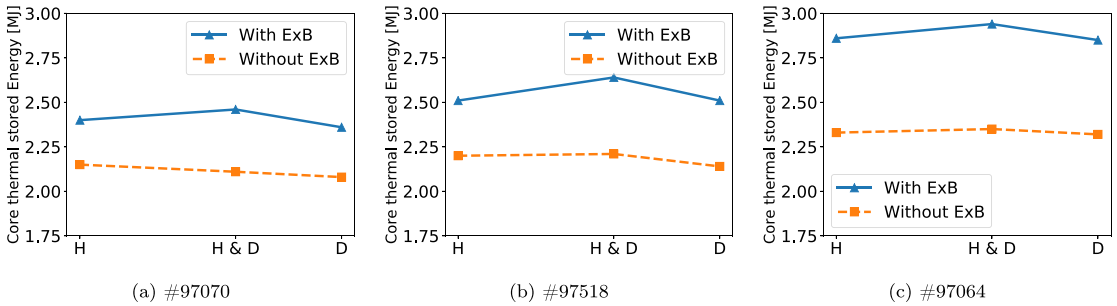

(a) #97070 (b) #97518 (c) #97064

Figure 19. Core thermal stored energy from the ETS simulations where the isotope mixture for the three discharges has been switched while using the same pedestal.

indicates that $E \times B$-shearing enhances the stored thermal energy in the core and that the magnitude of this enhancement increases with M_{eff}.

To quantify the agreement between simulations and experiment, we computed the averaged normalised mean absolute error (MAE):

$$\text{MAE} = \sum_{\text{i}} \frac{1}{3} \sum_{j} \frac{1}{n} \frac{|X_{ij,\text{exp}} - X_{ij,\text{ETS}}|}{X_{ij,\text{exp}}} \tag{3}$$

where 'i' represents the three profiles; electron density, ion and electron temperatures; 'j' represents the radial grid points ($n = 90$). The MAE-values for the two $E \times B$-cases: Rot = 1: MAE = 0.0815. Rot = 0: MAE = 0.144, confirming quantitatively that the inclusion of $E \times B$-shear substantially improves agreement with the experimental data.

As shown in table 4, the energy content in the core has a scaling proportional to $M_{\text{eff}}^{0.24}$ for the ETS simulations with TGLF. The linear GENE analysis suggested that both the pedestal height and external $E \times B$-shearing contribute to the positive isotope scaling. To disentangle their relative influence, additional ETS simulations were performed using fixed pedestal conditions while varying the isotope composition.

3.2.3. The influence of the pedestal height on core profiles

It is well established that turbulent transport in the plasma core often displays a threshold feature, [56, 57], meaning that the fluxes remain small below a critical value of a gradient, typically of the temperature, but increases sharply once this threshold is exceeded. Consequently, the normalised gradients across the core tend to stay close to this critical value, which is often referred to as the profiles exhibit a stiff behaviour. If the critical threshold itself is unaffected by the variation of the pedestal height, one would expect predictive integrated modelling simulations to result in profiles with similar normalised gradients whether or not the pedestal are increased. Below the importance of this effect for the analysed discharges is investigated.

Each discharge was used as a 'base case', in which the pedestal, rotation, and equilibrium were held fixed while the isotope mixture was systematically varied. For example, the hydrogen discharge (#97070 (H)) was re-simulated using the isotope ratios of the mixed and deuterium cases. These tests were carried out both with and without $E \times B$ shearing, and the resulting core stored energies are shown in figure 19. The results show very little change in stored energy with isotope mass when the pedestal is fixed, irrespective of whether $E \times B$-shearing is included. If core transport were governed solely by gyro-Bohm scaling, an inverse dependence on mass would be expected. To clarify these findings, we focus on the simulations using the pedestal from the nearly pure hydrogen discharge (#97070(H)), with different isotope mixtures. These are indicated by the blue line and triangles in figure 19(a). The corresponding temperature and electron density profiles, along with their normalised gradients, are presented in figure 20, with the labels indicating the isotope mixture. From the temperature and density profiles, it is evident that changing the isotope composition has only a minor effect on the fluxes. This is further indicated by the normalised gradients, they are very similar for all isotope mixtures. This resilience of the profiles stems from the stiffness of the turbulent transport. Regardless of the isotope mixtures we end up with the same normalised gradients.

In a similar manner, we investigate the effect of the pedestal on the core stored energy, independent of the internal isotope scaling in TGLF. Simulations were performed using identical isotope mixtures while varying only the pedestal conditions. The resulting core stored thermal energies, with and

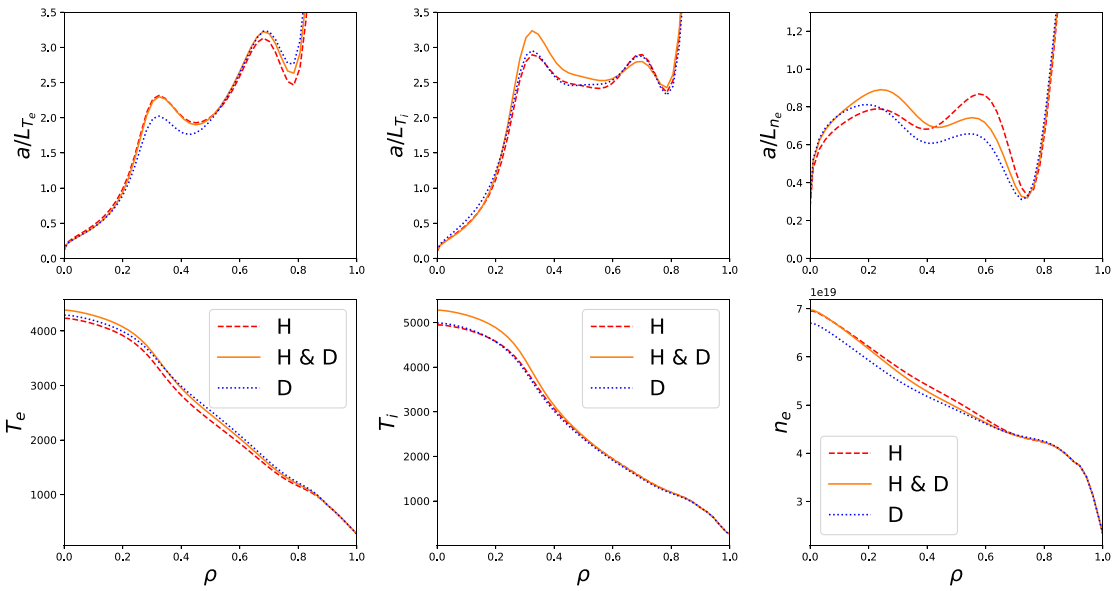

Figure 20. Normalised gradients for the electron temperature (left), ion temperature (middle) and electron density (right) from the predictive ETS simulations presented in figure 19(a) with $E \times B$. All three simulations were performed with pedestal of the hydrogen discharge #97070 and only differ for the isotope mixture.

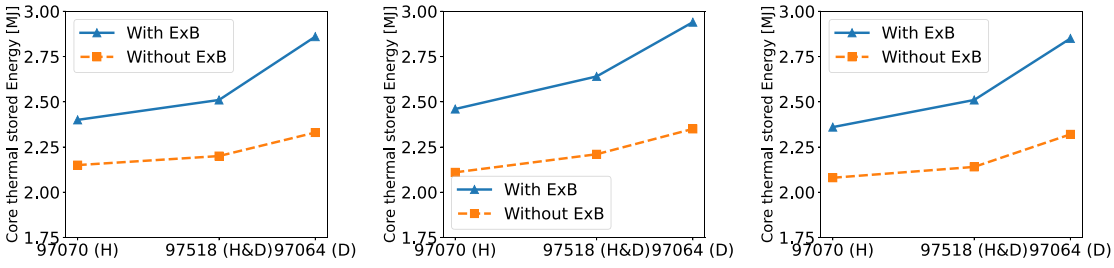

(a) H (b) H & D (c) D

Figure 21. Core thermal stored energy from the ETS simulations where the pedestal for the three discharges has been switched.

without $E \times B$-shearing, are presented in figure 21. In both cases, the stored thermal energy increases with a higher pedestal, scaling as $\sim M_{\text{eff}}^{0.24}$ with $E \times B$-shearing and $\sim M_{\text{eff}}^{0.13}$ without. The scaling found with external $E \times B$-shearing is identical to that obtained in the ETS simulations used to obtain table 4, where each discharge has its own pedestal. This demonstrates that the isotope-dependent pedestal exerts a dominant influence on the core stored energy through the stiff behaviour of the plasma profiles. The consequence is that modifying the pedestal does not significantly change the normalised gradients of the profiles; meaning that a higher pedestal leads to more pronounced peaking. This is illustrated by the simulations using hydrogen, $E \times B$-hearing, and different pedestal heights-the blue line with triangles in figure 21(a). The corresponding profiles and normalised gradients for these three simulations are shown in figure 22. The temperature and density profiles in the lower panels display the effect of lifting the pedestal in the edge region. Despite the different pedestal heights, the normalised gradients remain very similar, indicating increased profile peaking at a higher pedestal.

It is important to point out that while these results are not inconsistent with the linear GENE results discussed in section 3.1.6, they cannot be inferred from a linear analysis since they require the profiles to evolve self-consistently. Overall, the ETS results indicate that the pedestal height, through its effect on the normalised density and temperature gradients, together with the stiff behaviour of the profiles, plays the primary role in the observed positive isotope scaling of core confinement. The core thermal stored energy follows the trend of the pedestal stored energy: an increase in the latter leads directly to an increase in the former.

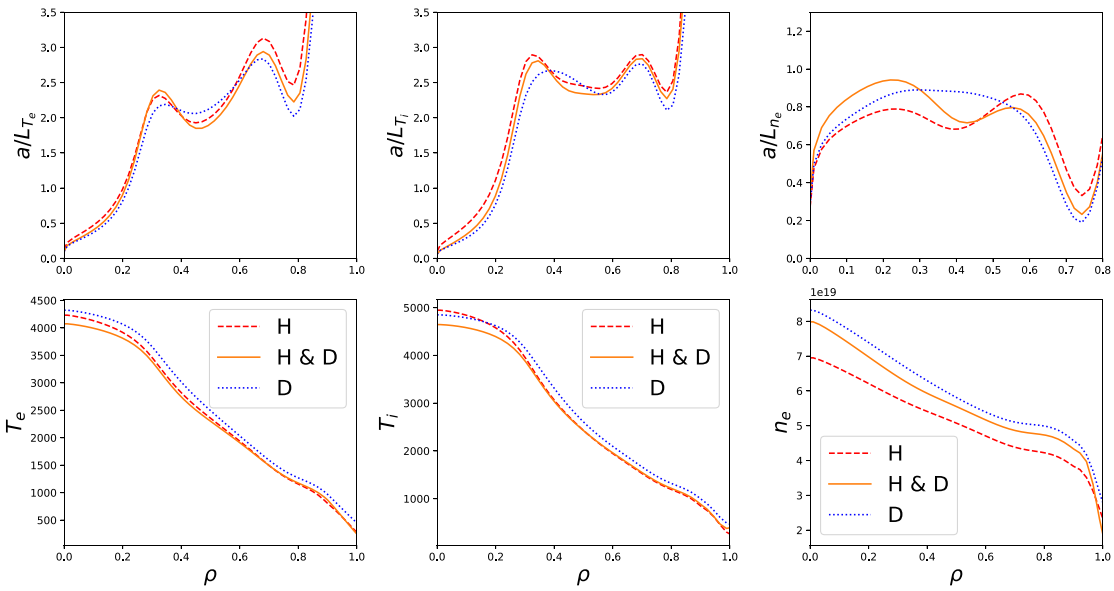

Figure 22. Normalised gradients for the electron temperature (left), ion temperature (middle) and electron density (right) from the predictive ETS simulations presented in figure 21(a) with $E \times B$. All three simulations were performed with hydrogen and only differ for the pedestal. H indicates pedestal from #97070 (lowest pedestal), H&D #97518 and D #97064 (highest).

4. Conclusions

This study examined three JET discharges aimed at studying the influence of the main ion mass on the stored thermal energy. The discharges were matched in engineering parameters rather than in dimensionless physics parameters, adding complexity to their interpretation. All three discharges were in the H-mode regime. Analysis of the experimental profiles showed that both the pedestal and core thermal stored energies increased with the effective ion mass, M_{eff}. The observed improvement in core thermal stored energy with increasing M_{eff} motivated a detailed investigation of the underlying physical mechanisms responsible for the positive isotope scaling.

Linear gyrokinetic simulations using the GENE code demonstrated that, when all plasma parameters (including normalised gradients) were held constant and only M_{eff} was varied, the growth rates followed the expected gyro-Bohm scaling reasonably well. To explain the experimental observations, three potential mechanisms were investigated: (i) the influence of the variation of pedestal height with M_{eff} on core profiles, as they show a stiff behaviour in integrated simulations; (ii) $E \times B$-shearing due to the externally driven plasma rotation (i.e. due to the input torque from the NBI heating); and (iii) the presence of ETG-modes. Based on linear analysis, the combined influence of $E \times B$ shearing and the pedestal effect appears to account for the experimentally observed positive scaling of core energy confinement with plasma mass, consistent with previous studies [19, 24, 25, 31, 58]. However, linear results can only indicate the relative strength of the underlying mechanisms. Non-linear turbulence dynamics and the complex interdependence of the plasma profiles make it difficult to determine the direct relevance of linear analysis on the resulting profiles. For this reason, integrated modelling with ETS and TGLF was carried out to better assess the effects on the profiles. These simulations showed that the influence of $E \times B$ shearing was weaker than suggested by the linear analysis, and that the pedestal-through the stiff behaviour of the profiles in the integrated simulations-plays the dominant role in governing the scaling of the core stored energy with ion mass. The analysis of the impact of ETG-modes shows that only one of the three discharges exhibits a significant contribution to the electron heat flux from ETG turbulence. This suggests that ETG-modes do not play a major role in the observed positive mass scaling. The integrated simulations with ETS reproduced the experimental trend of increasing core energy with M_{eff}, albeit with somewhat weaker scaling.

The main conjecture emerging from the presented analysis is that in the investigated discharges, the main cause of the isotope mass scaling of the core thermal stored energy was the variation of the pedestal properties combined with profiles stiffness. Integrated modelling essentially showed that the same normalised gradients were obtained regardless of the isotope composition or pedestal height. Consequently, the core thermal stored energy reflects the behaviour of the pedestal stored energy: an increase in the pedestal leads directly to an increase in the core stored energy.

Acknowledgments

This work has been carried out within the framework of the EUROfusion Consortium, funded by the European Union via the Euratom Research and Training Programme (Grant Agreement No 101052200 —EUROfusion). Views and opinions expressed are however those of the author(s) only and do not necessarily reflect those of the European Union or the European Commission. Neither the European Union nor the European Commission can be held responsible for them.

Data availability statement

The data cannot be made publicly available upon publication due to legal restrictions preventing unrestricted public distribution. The data that support the findings of this study are available upon reasonable request from the authors.

ORCID iDs

E Fransson 0000-0002-8747-3470
L-G Eriksson 0009-0004-1375-9929
P Strand 0000-0002-8899-2598
E Viezzer 0000-0001-6419-6848

References

[1] Strachan J D *et al* 1997 TFTR DT experiments *Plasma Phys. Control. Fusion* **39** B103
[2] Keilhacker M, Windsor C, Keilhacker M, Lawson J D, Pert G J and Robinson D C 1999 JET deuterium: tritium results and their implications *Phil. Trans. R. Soc. A* **357** 415
[3] Maggi C F 2023 Foreword to the nuclear fusion special issue of papers presenting results from the JET tritium and deuterium / tritium campaign *Nucl. Fusion* **63** 110201
[4] Kappatou A *et al* 2025 Overview of the third JET deuterium-tritium campaign *Plasma Phys. Control. Fusion* **67** 045039
[5] Liewer P C 1985 Measurements of microturbulence in tokamaks and comparisons with theories of turbulence and anomalous transport *Nucl. Fusion* **25** 543–621
[6] Horton W 1999 Drift waves and transport *Rev. Mod. Phys.* **71** 735–78
[7] ITER Physics Basis ed et al ITER Physics Basis Expert Groups on Confinement and Transport and Confinement Modelling and Database 1999 *Nucl. Fusion* **39** 2175
[8] Petty C C *et al* 1995 Nondimensional transport scaling in DIII-D: Bohm versus gyro-Bohm resolved *Phys. Plasmas* **2** 2342–8
[9] Cordey J G *et al* 1996 A review of the dimensionless parameter scaling studies *Plasma Phys. Control. Fusion* **38** A67
[10] Cordey J G 1999 H mode power threshold and confinement in JET H, D, DT and T *plasmas Nucl. Fusion* **39** 1763
[11] Frassinetti L *et al* 2021 Pedestal structure, stability and scalings in JET-ILW: the EUROfusion JET-ILW pedestal database *Nucl. Fusion* **61** 016001
[12] Maggi C F *et al* 2018 Isotope effects on L-H threshold and confinement in tokamak plasmas *Plasma Phys. Control. Fusion* **60** 014045
[13] Horvath L *et al* 2021 Isotope dependence of the type I ELMy H-mode pedestal in JET-ILW hydrogen and deuterium plasmas *Nucl. Fusion* **61** 046015
[14] Frassinetti L *et al* 2023 Effect of the isotope mass on pedestal structure, transport and stability in D, D/T and T plasmas at similar β_N and gas rate in JET-ILW type I ELMy H-modes *Nucl. Fusion* **63** 112009
[15] Laggner F M *et al* 2017 Pedestal structure and inter-ELM evolution for different main ion species in ASDEX Upgrade *Phys. Plasmas* **24** 056105
[16] Schneider P A, Hennequin P, Bonanomi N, Dunne M, Conway G D and Plank U 2022 Overview of the isotope effects in the ASDEX Upgrade tokamak *Plasma Phys. Control. Fusion* **63** 064006
[17] Urano H and Narita E 2021 Review of hydrogen isotope effects on H-mode confinement in JT-60U *Plasma Phys. Control. Fusion* **63** 084003
[18] Angioni C, Fable E, Manas P, Mantica P and Schneider P A 2018 Dependence of the turbulent particle flux on hydrogen isotopes induced by collisionality *Phys. Plasmas* **25** 082517
[19] Weisen H *et al* 2020 Isotope dependence of energy, momentum and particle confinement in tokamaks *J. Plasma Phys.* **86** 905860501
[20] Ernst D R *et al* 1998 Unifying role of radial electric field shear in the confinement trends of TFTR supershot plasmas *Phys. Rev. Lett.* **81** 21
[21] Garcia J *et al* 2022 Modelling and theoretical understanding of the isotope effect from JET experiments in view of reliable predictions for deuterium-tritium plasmas *Plasma Phys. Control. Fusion* **64** 054001
[22] Garcia J, Görler T, Jenko F and Giruzzi G 2017 Gyrokinetic nonlinear isotope effects in tokamak plasmas *Nucl. Fusion* **57** 014007
[23] Casson F J *et al* 2020 Predictive multi-channel flux-driven modelling to optimise ICRH tungsten control and fusion performance in JET *Nucl. Fusion* **60** 066029
[24] Bateman G, Kritz A H, Parail V V and Cordey J G 1999 Effect of isotope mass on transport simulations of joint European torus highmode plasmas with edge localized modes *Phys. Plasmas* **6** 4607

[25] Schneider P A et al 2022 The dependence of confinement on the isotope mass in the core and the edge of AUG and JET-ILW H-mode plasmas Nucl. Fusion 62 026014
[26] Schneider P A et al 2023 Isotope physics of heat and particle transport with tritium in JET-ILW type-I ELMy H-mode plasmas Nucl. Fusion 63 112010
[27] Bustos A, Bañón Navarro A, Görler T, Jenko F and Hidalgo C 2015 Microturbulence Study of the isotope effect Phys. Plasmas 22 012305
[28] Hahm T S, Wang L, Wang W X, Yoon E S and Duthoit F X 2013 Isotopic dependence of residual zonal flows Nucl. Fusion 53 072002
[29] Nakata M, Nunami M, Sugama H and Watanabe T-H 2017 Isotope effects on trapped-electron-mode driven turbulence and zonal flows in helical and tokamak plasmas Phys. Rev. Lett. 118 165002
[30] Idomura Y 2019 Isotope and plasma size scaling in ion temperature gradient driven turbulence Phys. Plasmas 26 120703
[31] Maggi C F et al 2019 Isotope identity experiments in JET-ILW with H and D L-mode plasmas Nucl. Fusion 59 076028
[32] King D et al 2020 Mixed hydrogen-deuterium plasmas on JET ILW Nucl. Fusion 60 096030
[33] Imbeaux F et al 2015 Design and first applications of the ITER integrated modelling & analysis suite Nucl. Fusion 55 123006
[34] Ho A, Citrin J, Auriemma F, Bourdelle C, Casson F J, Kim H-T, Manas P, Szepesi G and Weisen H 2019 Application of Gaussian process regression to plasma turbulent transport model validation via integrated modelling Nucl. Fusion 59 056007
[35] Rasmussen C and Williams C 2006 Gaussian Processes for Machine Learning (MIT Press)
[36] Jenko F and Dorland W 2001 Dorland Nonlinear electromagnetic gyrokinetic simulations of tokamak plasmas Plasma Phys. Control. Fusion 43 A141–50
[37] Lao L L, St. John H, Stambaugh R D, Kellman A G and Pfeiffer W 1985 Reconstruction of current profile parameters and plasma shapes in tokamaks Nucl. Fusion 25 1611
[38] Appel L et al 2006 3rd EPS Conf. (Rome) p 2.184
[39] Appel L and Lupelli I 2018 Equilibrium reconstruction in an iron core tokamak using a deterministic magnetisation model Comput. Phys. Commun. 223 1–17
[40] Merz F 2008 Gyrokinetic simulation of multimode plasma turbulence PhD Thesis Universitat Munster
[41] Coster D, Basiuk V, Pereverzev G, Kalupin D, Zagorksi R, Stankiewicz R, Huynh P and Imbeaux F 2010 The European transport solver IEEE Trans. Plasma Sci. 38 9
[42] Kalupin D et al 2013 Numerical analysis of JET discharges with the European transport simulator Nucl. Fusion 53 123007
[43] Staebler G M, Kinsey J E and Waltz R E 2005 Gyro-Landau fluid equations for trapped and passing particles Phys. Plasmas 12 102508
[44] Staebler G M, Belli E A, Candy J, Kinsey J E, Dudding H and Patel B 2021 Verification of a quasi-linear model for gyrokinetic turbulent transport Nucl. Fusion 61 116007
[45] Houlberg W A, Shaing K C, Hirshman S P and Zarnstorff M C 1997 Bootstrap current and neoclassical transport in tokamaks of arbitrary collisionality and aspect ratio Phys. Plasmas 4 3230
[46] Schneider M, Eriksson L-G, Jenkins I, Artaud J F, Basiuk V, Imbeaux F and Oikawa T 2011 Simulation of the neutral beam deposition within integrated tokamak modelling frameworks Nucl. Fusion 51 063019
[47] Staebler G, Bourdelle C, Citrin J and Waltz R 2024 Quasilinear theory and modelling of gyrokinetic turbulent transport in tokamaks Nucl. Fusion 64 103001
[48] Hein T, Angioni C, Fable E and Candy J 2010 Gyrokinetic study of β the role of on electron particle transport in tokamaks Phys. Plasmas 17 102309
[49] Pusztai I et al 2011 Isotope mass and charge effects in tokamak plasmas Phys. Plasmas 18 122501
[50] Staebler G M, Howard N T, Candy J and Holland C 2017 A model of the saturation of coupled electron and ion scale gyrokinetic turbulence Nucl. Fusion 57 066046
[51] Creely A J, Rodriguez-Fernandez P, Conway G D, Freethy S J, Howard N T and White A E 2019 Criteria for the importance of multi-scale interactions in turbulent transport simulations Plasma Phys. Control. Fusion 61 085022
[52] Mantica P et al 2021 The role of electron-scale turbulence in the JET tokamak: experiments and modelling Nucl. Fusion 61 096014
[53] Citrin J et al 2022 Integrated modelling and multiscale gyrokinetic validation study of ETG turbulence in a JET hybrid H-mode scenario Nucl. Fusion 62 086025
[54] Waltz R E, Staebler G M, Dorland W, Hammett G W, Kotschenreuther M and Konings J A 1997 A gyro-Landau-fluid transport model Phys. Plasmas 4 2482
[55] Hahm T S and Burell K 1995 Low shear induced fluctuation suppression in finite aspect ratio shaped tokamak plasma Phys. Plasmas 2 1648
[56] Mantica P et al 2009 Experimental study of the ion critical-gradient length and stiffness level and the impact of rotation in the JET Tokamak Phys. Rev. Lett. 102 175002
[57] Yoshida M et al 2025 Transport and confinement physics: chapter 2 of the special issue: on the path to tokamak burning plasma operation Nucl. Fusion 65 033001
[58] Garcia J et al 2019 First principles and integrated modelling achievements towards trustful fusion power predictions for JET and ITER Nucl. Fusion 59 086047